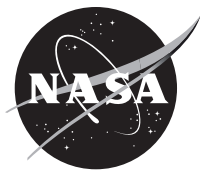# An Ensemble Neural Network Model for Predicting Rare-Earth Oxide and Silicate Heat Capacities at High Temperature

Cameron J. Bodenschatz
Glenn Research Center, Cleveland, Ohio

NASA STI Program . . . in Profile

Since its founding, NASA has been dedicated to the advancement of aeronautics and space science. The NASA Scientific and Technical Information (STI) Program plays a key part in helping NASA maintain this important role.

The NASA STI Program operates under the auspices of the Agency Chief Information Officer. It collects, organizes, provides for archiving, and disseminates NASA's STI. The NASA STI Program provides access to the NASA Technical Report Server—Registered (NTRS Reg) and NASA Technical Report Server—Public (NTRS) thus providing one of the largest collections of aeronautical and space science STI in the world. Results are published in both non-NASA channels and by NASA in the NASA STI Report Series, which includes the following report types:

- TECHNICAL PUBLICATION. Reports of completed research or a major significant phase of research that present the results of NASA programs and include extensive data or theoretical analysis. Includes compilations of significant scientific and technical data and information deemed to be of continuing reference value. NASA counter-part of peer-reviewed formal professional papers, but has less stringent limitations on manuscript length and extent of graphic presentations.

- TECHNICAL MEMORANDUM. Scientific and technical findings that are preliminary or of specialized interest, e.g., "quick-release" reports, working papers, and bibliographies that contain minimal annotation. Does not contain extensive analysis.

- CONTRACTOR REPORT. Scientific and technical findings by NASA-sponsored contractors and grantees.

- CONFERENCE PUBLICATION. Collected papers from scientific and technical conferences, symposia, seminars, or other meetings sponsored or co-sponsored by NASA.

- SPECIAL PUBLICATION. Scientific, technical, or historical information from NASA programs, projects, and missions, often concerned with subjects having substantial public interest.

- TECHNICAL TRANSLATION. English-language translations of foreign scientific and technical material pertinent to NASA's mission.

For more information about the NASA STI program, see the following:

- Access the NASA STI program home page at http://www.sti.nasa.gov

- E-mail your question to help@sti.nasa.gov

- Fax your question to the NASA STI Information Desk at 757-864-6500

- Telephone the NASA STI Information Desk at 757-864-9658

- Write to:
  NASA STI Program
  Mail Stop 148
  NASA Langley Research Center
  Hampton, VA 23681-2199

An Ensemble Neural Network Model for Predicting Rare-Earth Oxide and Silicate Heat Capacities at High Temperature

Cameron J. Bodenschatz
Glenn Research Center, Cleveland, Ohio

National Aeronautics and
Space Administration

Glenn Research Center
Cleveland, Ohio 44135

June 2023

Acknowledgments

An Ensemble Neural Network Model for Predicting Rare-Earth Oxide and Silicate Heat Capacities at High Temperature

Cameron J. Bodenschatz
National Aeronautics and Space Administration
Glenn Research Center
Cleveland, Ohio 44135

Summary

In this work, a neural network model was developed to predict the constant-pressure heat capacity C_p for materials in the RE_2O_3-SiO_2 material space (RE is a rare-earth metal). Several model architectures were trained and tested on C_p data generated from first-principles density functional theory (DFT) calculations. Hyperparameter optimization was performed, and the optimal model was selected for C_p predictions. The optimal model architecture was found to have a root-mean-squared error of 5.12 ± 3.37 J/mol-K. The optimal model architecture was then used in a bagging ensemble model that was trained using the leave-one-group-out method to provide error estimates for model predictions. The out-of-bag score for the ensemble model was 0.997. The predicted C_p values agree well with the DFT and experimental results and were computed orders of magnitude faster than DFT simulations. Machine learning shows the potential to provide a suitable surrogate model for thermochemical property predictions for candidate environmental barrier coating materials, but refining input material features and model architectures could further improve accuracy for these models.

1.0   Introduction

High-temperature stability of ceramic coatings, specifically rare-earth silicates, is an important design criterion for gas turbine aeroengines. Aeroengines are a challenging use case because of the extremely high temperatures inside the combustion chamber, especially as the aerospace industry pushes to increase combustion temperatures to improve fuel efficiency. As part of the push to increase efficiency, original equipment manufacturers (OEMs) have begun to replace traditional superalloy components with Si-based ceramic-matrix-composites (CMCs) of higher temperature capability and lower density (Refs. 1 and 2). However, CMCs are prone to degradation at high temperatures in environments containing water vapor or other oxidizing species (Refs. 3 and 4). Therefore, much research effort has gone into development of environmental barrier coatings (EBCs) to prevent CMC recession in jet engine environments. However, EBCs are prone to failure via a variety of mechanisms including oxidation, recession, spallation, and foreign object damage. Volumetric contraction or expansion due to phase transitions in engine operating conditions can also lead to mechanical failure of EBCs (Ref. 5). Rare-earth disilicates ($RE_2Si_2O_7$) have been a primary focus for EBC research because of their favorable coefficient of thermal expansion (CTE) match with the underlying Si-based CMC component substrate and their chemical stability in high-temperature water-vapor environments.

Coating design is challenging because of the large chemical space of candidate materials and the dearth of available properties for design calculations. Also, rare-earth silicates can form a variety of crystal structures, each of which has unique phase stability under various operating conditions. This challenge is compounded as research into more exotic materials such as solid-solution and so-called high-entropy ceramics has recently increased. As such, the use of chemical thermodynamics via methods such as the calculation of phase diagrams (CALPHAD) enables the exploration of the chemical space for rare-

earth-silicate EBC candidate materials. However, phase diagram calculations using the CALPHAD method require thermodynamic values of the materials of interest as inputs. Some of these values are available experimentally or in the literature, but others are not. Some quantities, such as entropies, are difficult to determine experimentally and must be calculated using computational methods. Current thermochemical properties calculations for candidate materials are primarily limited to density functional theory (DFT) calculations (Refs. 6 to 11). While DFT has proven highly capable, these calculations require substantial computational resources. As such, researchers are limited in the types of properties they can calculate. This report focuses on constant-pressure heat capacity, C_p, because of its importance in CALPHAD calculations.

Machine learning (ML) approaches to predict materials properties have seen substantial development over the past decade. Advancements in ML for materials include feature descriptor development, model development, and interatomic potentials for molecular dynamics (MD) simulations. Supervised learning regression models to predict single properties for a broad chemical space have been implemented into software packages including SchNetPack (Ref. 12), MEGNET (Ref. 13), and CGCNN (Ref. 14). In many studies, properties such as thermal expansion have been correlated to various rare-earth cation properties, including the ionic radius of the rare-earth cation and/or the geometry of the crystal cell (Refs. 6 and 15 to 20). This is likely because of the dependence of cell volume on the phonon frequencies within the quasi-harmonic approximation of lattice vibrations, which plays a key role in the transfer of heat through a material (Refs. 20 and 21). Some of the feature descriptors used in this work are included with this in mind. ML models have been developed for EBC thermomechanical properties such as CTE, using similar input feature properties (Ref. 6). However, this work focuses on the use of ML models for EBC thermochemical properties. This model could therefore be used, for example, as a surrogate model in thermochemical codes to predict thermodynamic stability of candidate EBC materials, either for pure material phase stability or in the presence of chemical contaminants such as calcia-magnesia-alumina-silicates (CMAS).

2.0   Methods

2.1   Density Functional Theory

Plane-wave DFT simulations were performed using the Vienna Ab initio Simulation Package (VASP) (Refs. 22 to 25). Calculations employed a plane-wave cutoff energy of 520 eV and a k-space integration mesh of 1,500 k-points per reciprocal atom. Projector-augmented wave (PAW) pseudopotentials modeled the core electrons (Refs. 26 to 28), while the Perdew-Burke-Ernzerhof modified for solids (PBEsol) exchange-correlation functional modeled the valence electrons (Refs. 29 and 30). Initial structures were obtained from the Materials Project database (Ref. 31). Geometries were optimized to a maximum residual force tolerance of 1×10^{-4} eV/Å on any individual atom. Phonon vibrational modes and heat capacities were calculated via the finite-displacement method using the Phonopy package for the Python programming language and using VASP for the single-point energy calculation for the displaced structures (Ref. 32). Displaced structures were generated using 2×2×2 supercells. The quasi-harmonic approximation was used to model thermodynamic properties at non-equilibrium volumes (Ref. 33).

2.2 Machine Learning

Neural network models were constructed using the multilayer perceptron regressor (MLPR) as implemented in BaggingRegressor, the scikit-learn package for the Python programming language (Ref. 34). The initial, unoptimized structures from the Materials Project database (Ref. 31) were used for ML input. Two datasets were used to train parallel models: one with scaled data and one with unscaled data. For both datasets, the only categorical variable (space group) was transformed using one-hot encoding. For the scaled dataset, the numerical variables were scaled to a range of 0 to 1. MLPR hyperparameters were tuned using the grid search method. The MLPR algorithm minimizes the negative mean-squared error loss function during model training. Early stopping and leave-one-group-out cross-validation, where the data for each crystal structure were considered as a group, were used to minimize overfitting during hyperparameter optimization.

Error estimates were calculated using the bootstrapping method and sampling with replacement via BaggingRegressor. An ensemble of 50 MLPR models were trained using the parameters found from the grid search hyperparameter optimization. Each model was trained on a randomized subset of the C_p data, and the remaining out-of-bag (OOB) data were used as a test set to calculate model accuracy. The error bounds for the prediction capability of the ensemble model were determined by taking the mean and standard deviation of the 50 models comprising the ensemble.

3.0 Results

3.1 Correlation Matrix

A summary of the materials considered in this work is shown in Table I. A correlation matrix was calculated using the initial input descriptors to determine the strength of their effects on the predicted C_p. The correlation matrix can be seen in Figure 1. Larger absolute values indicate a stronger correlation, while smaller absolute values indicate a weaker correlation. Positive values indicate a positive correlation, while negative values indicate a negative correlation. The strongest prediction correlation is the temperature, with a correlation coefficient of 0.54. Rare-earth cation atomic number, rare-earth cation electronegativity, lattice parameter b, and lattice angle β all have correlation coefficient absolute values of less than 0.1, indicating weak correlations with C_p. Temperature has the strongest positive correlation of 0.54, whereas the lattice parameter a and the conventional cell volume have the strongest negative correlations of –0.47 and –0.43, respectively. In all the candidate rare-earth disilicates considered in this study, the α and γ angles are both 90°, so they have identical correlations with C_p. Additionally, the $P\overline{1}$ space group demonstrated a correlation of 1 to both the α and γ angles. Therefore, the γ angle and the $P\overline{1}$ space group feature columns were removed from the feature matrix for model training.

TABLE I.—COMPOUND AND STRUCTURE INFORMATION FOR MATERIALS USED FOR TRAINING AND TESTING ML MODELS.

[Initial structures were obtained from Materials Project database (Ref. 31).]

| Formula	MP-ID	Space group	a, Å	b, Å	c, Å	α, deg	β, deg	γ, deg	Volume, Å^3
Dy$_2$Si$_2$O$_7$	mp-17062	$P\bar{1}$	6.66	6.69	12.15	94.32	91.32	91.97	539.89
Er$_2$Si$_2$O$_7$	mp-7064	$C2/m$	6.86	9.00	4.77	90.00	102.08	90.00	288.08
Er$_2$Si$_2$O$_7$	mp-7624	$P2_1/c$	4.75	10.81	5.59	90.00	96.21	90.00	285.19
Gd$_2$Si$_2$O$_7$	mp-13775	$Pnma$	5.13	8.34	14.00	90.00	90.00	90.00	598.92
Ho$_2$Si$_2$O$_7$	mp-18662	$Pnma$	5.08	8.16	13.75	90.00	90.00	90.00	569.64
Ho$_2$Si$_2$O$_7$	mp-16809	$P\bar{1}$	6.64	6.67	12.12	94.28	91.49	92.11	534.64
Lu$_2$Si$_2$O$_7$	mp-7193	$C2/m$	6.77	8.87	4.76	90.00	102.24	90.00	279.43
Tb$_2$Si$_2$O$_7$	mp-17308	$P\bar{1}$	6.69	6.72	12.19	94.24	91.21	91.86	545.52
Tm$_2$Si$_2$O$_7$	mp-1095467	$C2/m$	6.83	8.94	4.76	90.00	102.09	90.00	284.59
Y$_2$Si$_2$O$_7$	mp-5652	$C2/m$	6.93	9.09	4.79	90.00	101.89	90.00	295.34
Yb$_2$Si$_2$O7	mp-4300	$C2/m$	6.86	9.29	4.91	90.00	102.24	90.00	306.02
Dy$_2$SiO$_5$	mp-752405	$P2_1/c$	6.75	6.90	9.14	90.00	105.87	90.00	409.89
Dy$_2$SiO$_5$	mp-768317	$C2/c$	14.54	6.82	10.52	90.00	122.18	90.00	882.80
Er$_2$SiO$_5$	mp-16993	$P2_1/c$	6.71	6.77	9.14	90.00	103.57	90.00	404.01
Gd$_2$SiO$_5$	mp-542831	$P2_1/c$	6.78	7.11	9.22	90.00	107.51	90.00	424.40
Lu$_2$SiO$_5$	mp-18195	$P2_1/c$	6.68	6.61	9.12	90.00	100.33	90.00	396.41
Lu$_2$SiO$_5$	mp-16969	$C2/c$	14.28	6.67	10.29	90.00	121.99	90.00	831.72
Y$_2$SiO$_5$	mp-554420	$P2_1/c$	6.75	6.96	9.14	90.00	106.38	90.00	411.81
Yb$_2$SiO$_5$	mp-17702	$C2/c$	15.83	6.37	11.21	90.00	128.30	90.00	887.26
Dy$_2$O$_3$	mp-2345	$Ia\bar{3}$	10.68	10.68	10.68	90.00	90.00	90.00	1216.81
Er$_2$O$_3$	mp-679	$Ia\bar{3}$	10.55	10.55	10.55	90.00	90.00	90.00	1174.40
Gd$_2$O$_3$	mp-643084	$C2/m$	14.45	3.58	8.83	90.00	100.78	90.00	448.57
Lu$_2$O$_3$	mp-1427	$Ia\bar{3}$	10.36	10.36	10.36	90.00	90.00	90.00	1113.46
Lu$_2$O$_3$	mp-556477	$C2/m$	13.77	3.39	8.42	90.00	100.47	90.00	386.72
Yb$_2$O$_3$	mp-2814	$Ia\bar{3}$	10.71	10.71	10.71	90.00	90.00	90.00	1228.92
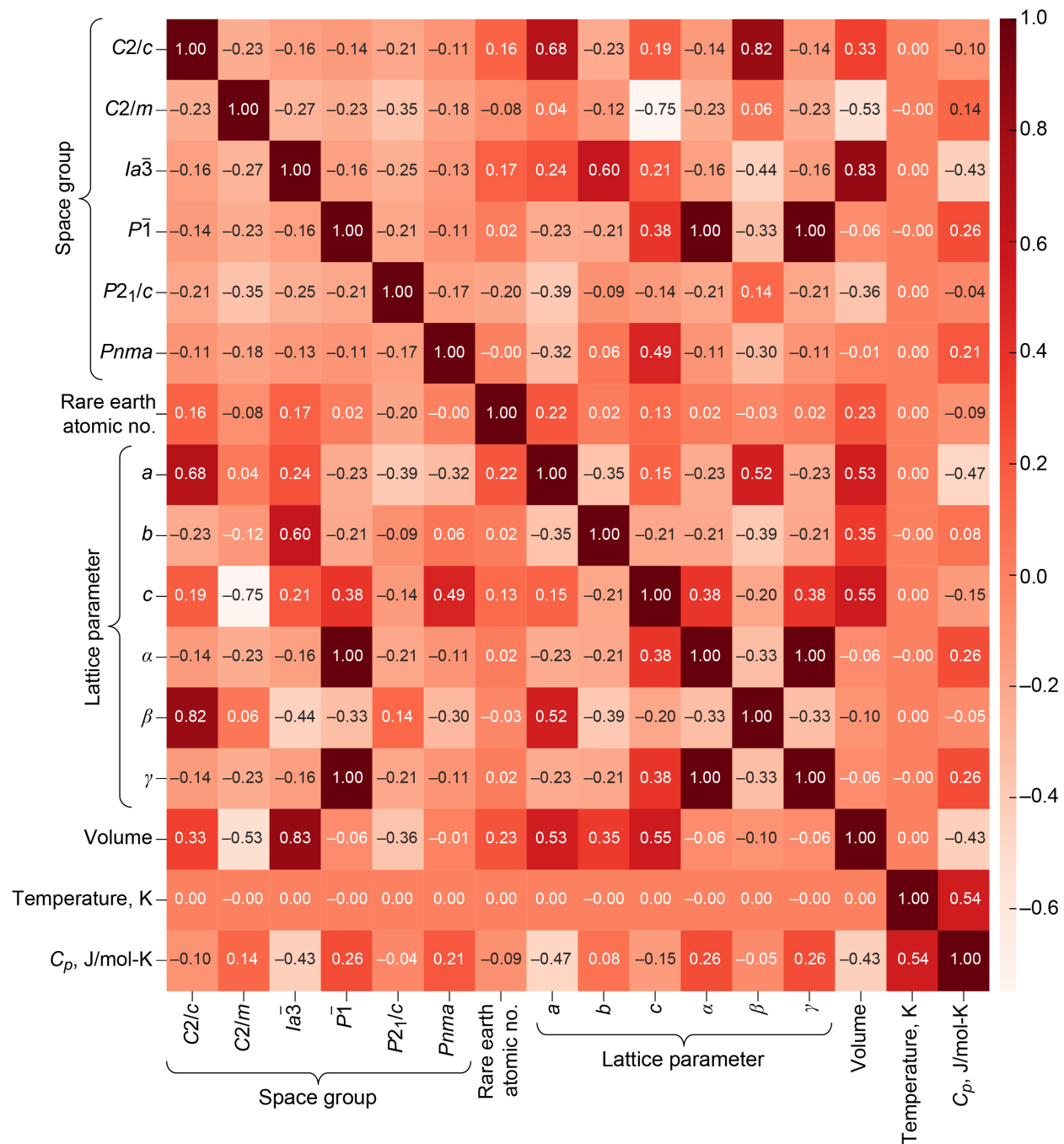
Figure 1.—Correlation matrix for input features to target C_p values of rare-earth silicate and oxide. Positive values indicate positive correlation, negative values indicate negative correlation, and values close to 0 indicate no correlation.

TABLE II.—HYPERPARAMETERS CONSIDERED FOR MODEL ARCHITECTURE
DURING HYPERPARAMETER OPTIMIZATION

Hidden layer sizes	(1), (10), (100), (1,1), (10,10), (100,100), (1000,1000), (1000,100), (10,10,10), (100,100,100), (1000,1000,1000), (1000,100,10)
Activation function	Logistic, RELU
Learning rate schedule	Constant, adaptive
L2 regularization strength coefficient	0.0001, 0.001, 0.01
Solver	LBFGS,[a] stochastic gradient descent, Adam
Maximum iterations	5,000
Iterations before early stopping	200

[a]Limited-memory Broyden-Fletcher-Goldfarb-Shanno optimization algorithm.

3.2   Hyperparameter Optimization

Hyperparameter optimization was performed using the grid search method and leave-one-group-out cross-validation to determine the optimal neural network model architecture. Variables considered in the hyperparameter optimization included number of hidden layers, size of hidden layers, L2 regularization strength coefficient, learning rate update method, activation function, and solver for a combined 288 unique model architectures. An overview of the hyperparameters used for model optimization can be seen in Table II. The negative mean-squared error was used as the scoring function during cross-validation. The best model was found to have an architecture of a single hidden layer with 100 neurons, adaptive learning with a L2 regularization strength coefficient of 0.01, the rectified linear unit (RELU) activation function, and the Adam solver. The mean-squared error of the model on the test dataset was converted to a root-mean-squared error (RMSE) to compare directly to the target C_p values. The optimized model architecture yielded an average RMSE of 5.12±3.37 J/mol-K.

Interestingly, the best model was found to use scaled feature data and unscaled target data, as the models trained on the unscaled data and scaled data (including features and target) both had both a larger RMSE and a larger standard deviation. The RMSE of the model trained on unscaled data was 6.57±4.40 J/mol-K, whereas the model trained on the fully scaled data was 11.98±23.55 J/mol-K. The optimized model trained on the unscaled data had the same architecture as the optimal model, whereas the model trained on the unscaled data had an architecture that included two hidden layers, the first with 1000 nodes and the second with 100 nodes (size (1000,100)), with all other hyperparameters the same.

It is important to note that not all models converged within the restricted number of iterations, but these models were discarded because of their apparent training difficulty. Scaling of the input features helped to minimize the number of models that did not converge.

3.3   Single-Model Prediction Accuracy

The optimal model found during hyperparameter optimization was trained to predict C_p. The loss as a function of training epochs of the optimized model is shown in Figure 2. Again, the loss function for the MLPR model is negative mean-squared error, so units are $(J/mol-K)^2$. The parity plot showing the DFT-calculated C_p data versus the MLPR-predicted data can be seen in Figure 3. In the parity plot, perfect predictive capability would be indicated by all the predicted data points having equal x and y values; that is, values falling on the line with a slope of 1. As can be seen in Figure 3, the MLPR model predicts the calculated C_p data with good accuracy. There is a small deviation at the high-C_p end of the plot because the C_p data for $Er_2Si_2O_7$ trends upward in the DFT data at high temperature. Because this is

the only material that displayed this upward trend at high temperature, the MLPR model did not learn this trend and therefore underpredicts its C_p. If other materials are added to the dataset that display this trend, the MLPR model would be more likely to learn this trend for materials that display it.
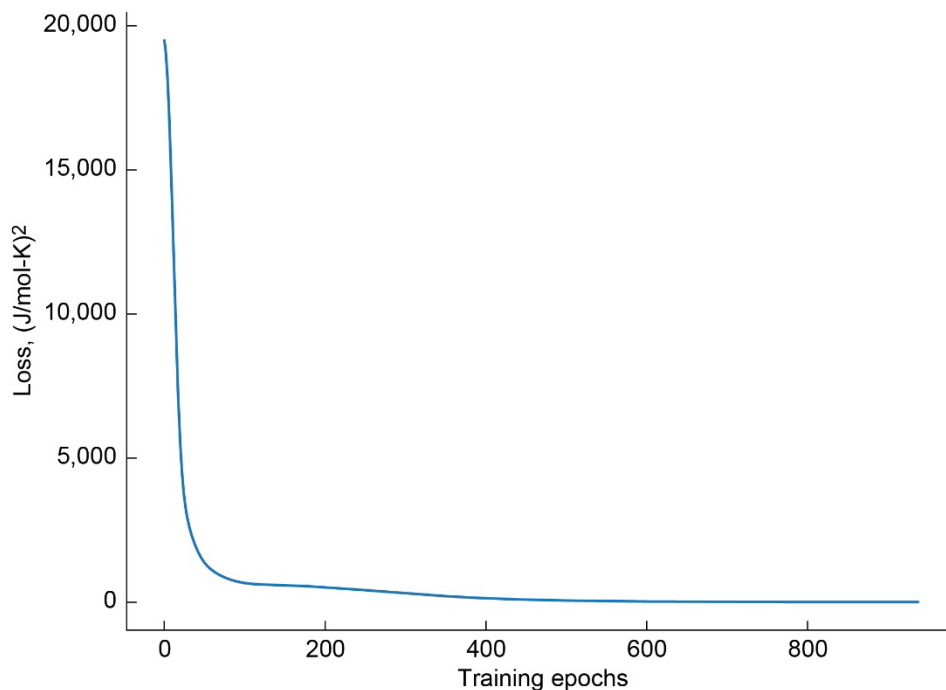

Figure 2.—The loss as a function of training epochs for a single MLPR model trained using the optimal architecture determined from grid search hyperparameter optimization.
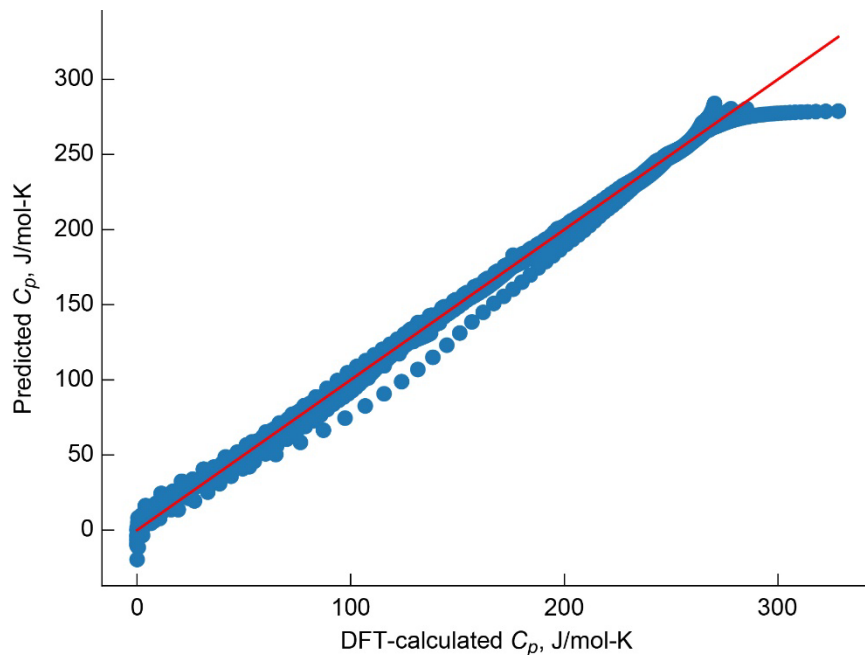

Figure 3.—Parity plot showing model prediction accuracy for C_p of rare-earth silicates compared to DFT results for single MLPR model using best parameters obtained from grid search hyperparameter optimization. Perfect predictive capability would result in all points falling on red line (slope = 1).

3.4 Ensemble-Model Prediction Accuracy

To establish an error range for the ML model, 50 models were trained to create an ensemble of models for statistical purposes. The OOB score for the ensemble model was 0.997. Each model in the ensemble was used to predict C_p of $Yb_2Si_2O_7$. The mean and standard deviation of the ensemble were then calculated for these predictions, and the prediction range can be seen in Figure 4. The average standard deviation for the ensemble-model C_p prediction across the entire temperature range is 1.1 eV. This error is lower than the RMSE for the model and therefore the model accuracy is limited by the model accuracy rather than the model variance. A parity plot of the C_p predictions for all materials in the dataset is shown in Figure 5. Although the model accuracy is likely insufficient for extremely accurate thermochemical calculations, it is likely sufficient for establishing trends or rough screening calculations. It is also possible that including additional sources of C_p data including experimental and literature data could improve the model accuracy.
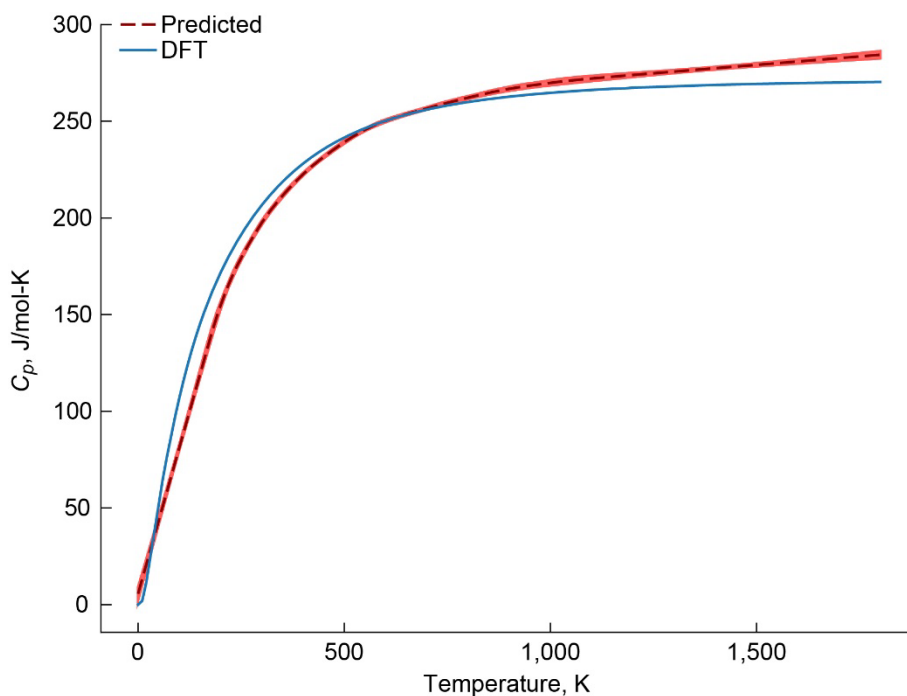

Figure 4.—Values of C_p for $Yb_2Si_2O_7$ predicted using ensemble model compared to those calculated with DFT. Dashed line indicates mean of 50 models comprising the ensemble, and shaded area represents first standard deviation.
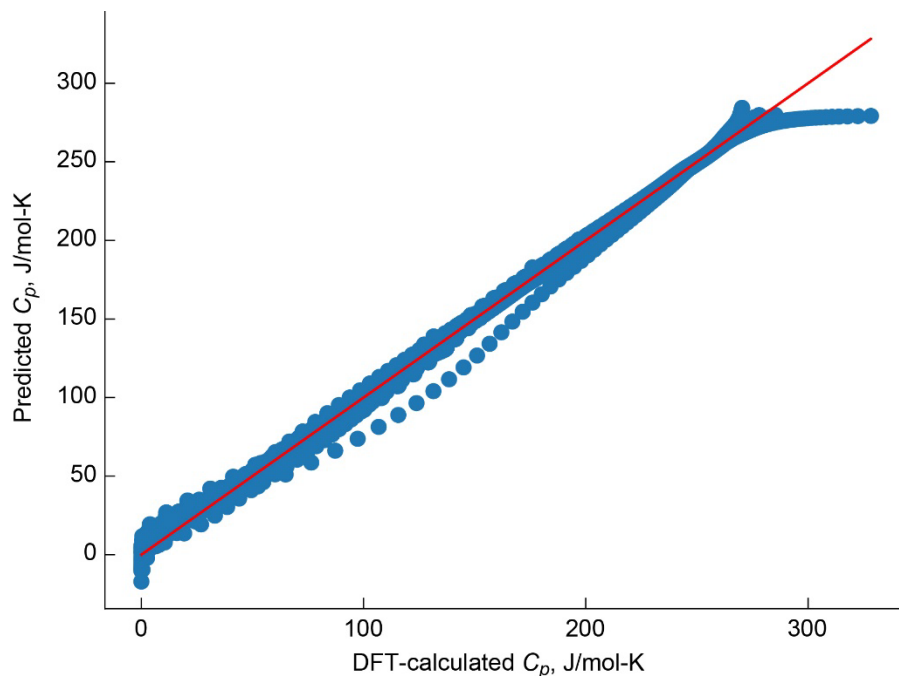
Figure 5.—Parity plot showing model prediction accuracy compared to DFT results of ensemble model for all materials in the dataset. Perfect predictive capability would result in all points falling on red line (slope = 1).

4.0   Discussion

To demonstrate the robustness of the model, the model was retrained using the optimal hyperparameters determined previously on the database, excluding values of C_p for $Yb_2Si_2O_7$. This allowed insight into the ability of the model to predict C_p for materials that were not included in the original dataset. There is only a minor loss of accuracy in the predicted C_p values compared to those predicted by the model that included $Yb_2Si_2O_7$ in the training dataset. This resulted in a slightly greater underprediction at temperatures in the lower end of the range (i.e., below 200 K) and a slightly greater overprediction at higher temperatures (i.e., above 1,000 K). Because it is likely that trends are more important than absolute predictions, this error may not influence coating design, but it points to the general robustness of the model. These results are shown in Figure 6.

The model was then used to predict C_p for structures not included in the dataset, including Nd and Sc disilicates. These materials are promising EBC candidate materials. The results are shown in Figure 7. These predicted C_p values are quite reasonable within the context of the C_p values of the other similar disilicate materials. However, we note that the predicted C_p values for $Sc_2Si_2O_7$ begin to decrease at high temperatures, which is likely an unrealistic result due to weaknesses in the model. This again indicates that while the model is likely sufficient for material screening purposes, it is inadequate for high-accuracy C_p calculations. However, it should be noted that C_p values for these materials were not found in the literature, so the model was able to provide predictions for materials where no data currently exists in a timeframe short enough for practical materials screening applications.
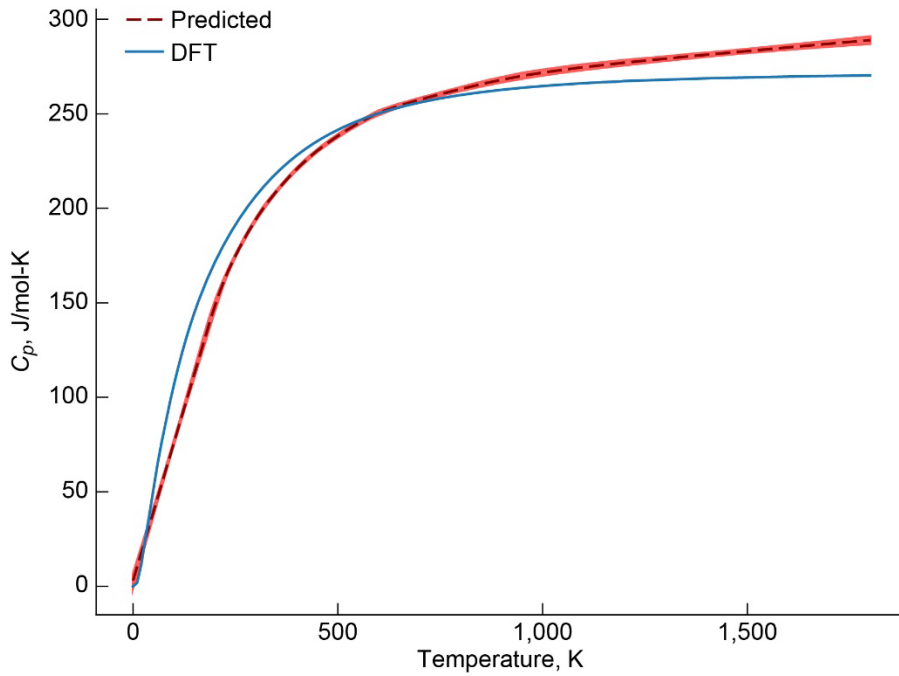
Figure 6.—Values of C_p for $Yb_2Si_2O_7$ predicted using ensemble model trained on all materials in dataset, excluding $Yb_2Si_2O_7$, compared to those calculated with DFT. Dashed line indicates mean of all 50 models comprising the ensemble, and shaded area represents first standard deviation.

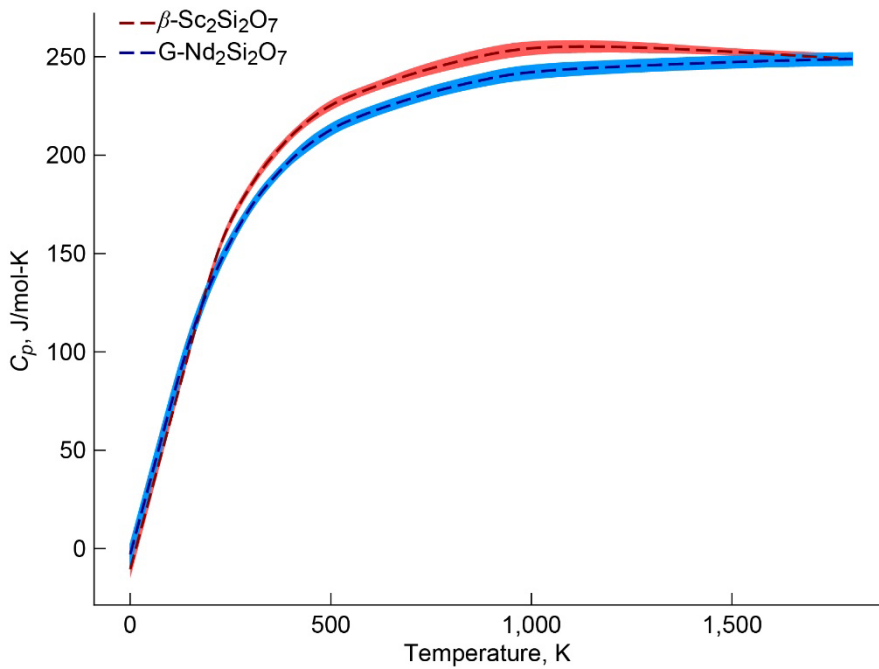Figure 7.—C_p predictions for β-$Sc_2Si_2O_7$ and G-$Nd_2Si_2O_7$ using the ensemble model trained on all materials in dataset. Dashed line indicates mean of all 50 models comprising the ensemble, and shaded area represents first standard deviation.

To improve the predictions on unseen materials and to enable additional capabilities such as mixed rare-earth silicate solid solutions, it is likely that additional feature information may need to be incorporated. One possible improvement could be the inclusion of local chemical environment information, such as nearest-neighbor bonding configurations, for the materials considered here in the input features. A variety of feature descriptors have been implemented in the literature to describe crystalline structures, including atom-centered symmetry functions (ACSF) (Refs. 35 and 36), smooth overlap of atomic positions (Ref. 37), and graph-based feature representations (Ref. 14). Several extensive reviews of feature representations for chemical descriptors have been recently published (Refs. 38 and 39). Crystal graphs have been used to develop ML models such as the Crystal Graph Convolutional Neural Network model by Xie and Grossman (Ref. 14), Chen et al. (Ref. 13), and others. These models use graph-based representations of the periodic crystal structure, where each node in the graph represents an atom and each edge represents a bond, to create a crystal graph for each material. These features are then fed into a convolutional neural network to develop a model that considers the local bonding environment of the constituent atoms in each material.

5.0 Conclusions

In this report, a neural network model was trained to predict heat capacities (C_p) in the RE_2O_3-SiO_2 chemical space (RE is a rare-earth metal). The model used the cell lattice parameters, the identity of the rare-earth cation, the space group, and the temperature as input features. The model was trained using a grid search to find the optimal model architecture, and the accuracy of the optimal model was determined using k-fold cross-validation to prevent model overfitting. The optimal model accuracy was found to be 5.12±3.37 J/mol-K. The model can predict C_p several orders of magnitude faster than density functional theory calculations (i.e., seconds as compared to days) and therefore could be used as a surrogate model for chemical thermodynamics calculations via, for example, the calculation of phase diagrams method. Although accuracy for materials not included in the training set was lower, the model likely produces results at sufficient accuracy for cursory screening applications. An improved feature matrix and/or an improved model architecture is likely needed for better predictions of C_p for materials out of the training set. Future model development can also focus on prediction of additional properties to guide environmental barrier coating design.

References

1. DiCarlo, James A.: Advances in SiC/SiC Composites for Aero-Propulsion. Ceramic Matrix Composites: Materials, Modeling and Technology. Ch. 7, Wiley Online Library, 2014, pp. 217–235.
2. Naslain, R.; and Christin, F.: SiC-Matrix Composite Materials for Advanced Jet Engines. MRS Bull., 2003, vol. 28, pp. 654–658.
3. Opila, Elizabeth J., et al.: SiC Recession Caused by SiO_2 Scale Volatility Under Combustion Conditions: II, Thermodynamics and Gaseous-Diffusion Model. J. Am. Ceram. Soc., vol. 82, no. 7, 1999, pp. 1826–1834.
4. Smialek, James L., et al.: SiC and Si_3N_4 Recession Due to SiO_2 Scale Volatility Under Combustor Conditions. Adv. Compos. Mater., vol. 8, no. 1, 1999, pp. 33–45.
5. Ito, J.; and Johnson, H.: Synthesis and Study of Yttrialite. Am. Mineral., vol. 53, nos. 11–12, 1968, pp. 1940–1952.

6. Ayyasamy, Mukil V., et al.: Density Functional Theory and Machine Learning Guided Search for $RE_2Si_2O_7$ With Targeted Coefficient of Thermal Expansion. J. Am. Ceram. Soc., vol. 103, no. 8, 2020, pp. 4489–4497.

7. Fujii, Susumu, et al.: Role of Phonons on Phase Stabilization of $RE_2Si_2O_7$ Over Wide Temperature Range (RE = Yb, Gd). J. Eur. Ceram. Soc., vol. 40, no. 3, 2020, pp. 780–788.

8. Wang, Yiguang; and Liu, Jinling: First-Principles Investigation on the Corrosion Resistance of Rare Earth Disilicates in Water Vapor. J. Eur. Ceram. Soc., vol. 29, no. 11, 2009, pp. 2163–2167.

9. Tian, Zhilin, et al.: Exploration of the Low Thermal Conductivities of γ-$Y_2Si_2O_7$, β-$Y_2Si_2O_7$, β-$Yb_2Si_2O_7$, and β-$Lu_2Si_2O_7$ as Novel Environmental Barrier Coating Candidates. J. Eur. Ceram. Soc., vol. 36, no. 11, 2016, pp. 2813–2823.

10. Luo, Yixiu, et al.: Material-Genome Perspective Towards Tunable Thermal Expansion of Rare-Earth Di-Silicates. J. Eur. Ceram. Soc., vol. 38, no. 10, 2018, pp. 3547–3554.

11. Xiang, Huimin; Feng, Zhihai; and Zhou, Yanchun: Mechanical and Thermal Properties of Yb_2SiO_5: First Principles Calculations and Chemical Bond Theory Investigations. J. Mater. Res., vol. 29, 2014, pp. 1609–1619.

12. Schutt, K.T., et al.: SchNet—A Deep Learning Architecture for Molecules and Materials. J. Chem. Phys., vol. 148, no. 24, 2018, p. 241722.

13. Chen, Chi, et al.: Graph Networks as a Universal Machine Learning Framework for Molecules and Crystals. Chem. Mater., vol. 31, no. 9, 2019, pp. 3564–3572.

14. Xie, Tian; and Grossman, Jeffrey C.: Crystal Graph Convolutional Neural Networks for an Accurate and Interpretable Prediction of Material Properties. Phys. Rev. Lett., vol. 120, no. 145301, 2018.

15. Felsche, J.: Polymorphism and Crystal Data of the Rare-Earth Disilicates of Type $R.E._2Si_2O_7$. J. Less Common Met., vol. 21, no. 1, 1970, pp. 1–14.

16. Dolan, M.D., et al.: Structures and Anisotropic Thermal Expansion of the α, β, γ, and δ Polymorphs of $Y_2Si_2O_7$. Powder Diffr., vol. 23, no. 1, 2008, pp. 20–25.

17. Fernandez-Carrion, Alberto J.; Allix, Mathieu; and Becerro, Ana I.: Thermal Expansion of Rare-Earth Pyrosilicates. J. Am. Ceram. Soc., vol. 96, no. 7, 2013, pp. 2298–2305.

18. Fukuda, Koichiro; and Matsubara, Hiroyuki: Thermal Expansion of δ-Yttrium Disilicate. J. Am. Ceram. Soc., vol. 87, no. 1, 2004, pp. 89–92.

19. Stokes, J.L., et al.: Crystal Structures and Thermal Expansion of $Yb_2Si_2O_7$–$Gd_2Si_2O_7$ Solid Solutions. J. Solid State Chem., vol. 312, no. 123166, 2022.

20. Stokes, J.L., et al.: Influence of Cation Species on Thermal Expansion of Y_2Si_2O7–$Gd_2Si_2O_7$ Solid Solutions. Submitted to J. Solid State Chem., 2023.

21. Dove, Martin T.: Introduction to Lattice Dynamics—Cambridge Topics in Mineral Physics and Chemistry, Series Number 4. Cambridge University Press, 1993.

22. Kresse, G.; and Furthmuller, J.: Efficiency of Ab-Initio Total Energy Calculations for Metals and Semiconductors Using a Plane-Wave Basis Set. Comput. Mater. Sci., vol. 6, no. 1, 1996, pp. 15–50.

23. Kresse, G.; and Furthmuller, J.: Efficient Iterative Schemes for Ab Initio Total-Energy Calculations Using a Plane-Wave Basis Set. Phys. Rev. B, vol. 54, no. 16, 1996, pp. 11169–11186.

24. Kresse, G.; and Hafner, J.: Ab Initio Molecular Dynamics for Liquid Metals. Phys. Rev. B, 1993, vol. 47, no. 1, pp. 558–561.

25. Kresse, G.; and Hafner, J.: Ab Initio Molecular-Dynamics Simulation of the Liquid Metal-Amorphous-Semiconductor Transition in Germanium. Phys. Rev. B, vol. 49, no. 20, 1994, pp. 14251–14269.

26. Kresse, G.; and Hafner, J.: Norm-Conserving and Ultrasoft Pseudopotentials for First-Row and Transition Elements. J. Phys.: Condens. Matter, vol. 6, no. 40, 1994, pp. 8245–8257.

27. Blochl, P.E.: Projector Augmented-Wave Method. Phys. Rev. B, vol. 50, no. 24, 1994, pp. 17953–17979.

28. Kresse, G.; and Joubert, D.: From Ultrasoft Pseudopotentials to the Projector Augmented-Wave Method. Phys. Rev. B, vol. 59, no. 3, 1999, pp. 1758–1775.

29. Perdew, John P.; Burke, Kieron; and Ernzerhof, Matthias: Generalized Gradient Approximation Made Simple. Phys. Rev. Lett., vol. 77, no. 18, 1996, pp. 3865–3868.

30. Perdew, John P., et al.: Restoring the Density-Gradient Expansion for Exchange in Solids and Surfaces. Phys. Rev. Lett., vol. 102, no. 13, 2008, p. 136406.

31. Jain, Anubhav, et al.: Commentary: The Materials Project: A Materials Genome Approach to Accelerating Materials Innovation. APL Mater., vol. 1, no. 1, 2013, p. 011002.

32. Togo, Atsushi; and Tanaka, Isao: First Principles Phonon Calculations in Materials Science. Scr. Mater., vol. 108, 2015, pp. 1–5.

33. Togo, Atsushi, et al.: First-Principles Phonon Calculations of Thermal Expansion in Ti_3SiC_2, Ti_3AlC_2, and Ti_3GeC_2. Phys. Rev. B, vol. 81, no. 17, 2010, p. 174301.

34. Pedregosa, Fabian, et al.: Scikitlearn: Machine Learning in Python. J. Mach. Learn. Res., vol. 12, 2011, pp. 2825–2830.

35. Behler, Jorg; and Parrinello, Michele: Generalized Neural-Network Representation of High-Dimensional Potential-Energy Surfaces. Phys. Rev. Lett., vol. 98, no. 14, 2007, p. 146401.

36. Behler, Jorg: Atom-Centered Symmetry Functions for Constructing High-Dimensional Neural Network Potentials. J. Chem. Phys., vol. 134, no. 7, 2011, p. 074106.

37. Bartok, Albert P.; Kondor, Risi; and Csanyi, Gabor: On Representing Chemical Environments. Phys. Rev. B, vol. 87, no. 18, 2013, p. 184115.

38. Musil, Felix, et al.: Physics-Inspired Structural Representations for Molecules and Materials. Chem. Rev., vol. 121, no. 16, 2021, pp. 9759–9815.

39. Li, Shunning, et al.: Encoding the Atomic Structure for Machine Learning in Materials Science. WIREs Comput. Mol. Sci., vol. 12, no. 1, 2022, p. e1558.